Asynchronous optical sampling of on-chip terahertz devices for real-time sensing and imaging applications

CONNOR D. W. MOSLEY,[1,*] ROBYN TUCKER,[1] JOSHUA P. R. NIXON,[1] SAEJUNE PARK,[2] LIANHE LI,[1] JOSHUA R. FREEMAN,[1] CHRISTOPHER D. WOOD,[1] EDMUND H. LINFIELD,[1] A. GILES DAVIES,[1] AND JOHN E. CUNNINGHAM[1]

[1]*School of Electronic and Electrical Engineering, University of Leeds, Leeds, West Yorkshire LS2 9JT, United Kingdom*
[2]*School of Electronic Engineering and Computer Science, Queen Mary University of London, London E1 4NS, United Kingdom*
*c.mosley@leeds.ac.uk

Abstract: We demonstrate that asynchronous optical sampling (ASOPS) can be used to measure the propagation of terahertz (THz) bandwidth pulses in a coplanar waveguide device with integrated photoconductive switches used for signal excitation and detection. We assess the performance of the ASOPS technique as a function of measurement duration, showing the ability to acquire full THz time-domain traces at rates up to 100 Hz. We observe a peak dynamic range of 40 dB for the shortest measurement duration of 10 ms, increasing to 88 dB with a measurement time of 500 s. Our work opens a route to real-time video-rate imaging via modalities using scanned THz waveguides, as well as real-time THz sensing of small volume analytes; we benchmark our on-chip ASOPS measurements against previously published simulations of scanning THz sensor devices, demonstrating sufficient dynamic range to underpin future video-rate THz spectroscopy measurements with these devices.

1. Introduction

Terahertz time-domain spectroscopy (THz-TDS) [1,2] is a powerful probe of material properties at THz frequencies, typically covering the spectral range from hundreds of GHz up to several THz. The non-ionising properties of THz radiation, paired with the non-contact nature of THz-TDS measurements, make this technique particularly attractive for applications in medical imaging [3–5]. THz-TDS has been applied to the delineation of tumour margins in skin [6] and breast [7] cancers, as well as imaging of skin conditions such as burns [8] and diabetic foot syndrome [9]. However, typical free-space THz-TDS systems suffer from bulky and cumbersome optics which, combined with the limited penetration depth of THz radiation in biological tissue [3,10], limits their applicability in medical imaging mainly to external, surface-based pathologies. On-chip THz spectroscopy schemes [11], consisting of lithographically-defined planar THz waveguides with integrated photoconductive switches for THz signal excitation and detection, provide a potential solution to the limitations of free-space systems. The compact nature of on-chip THz devices means they can potentially be integrated into existing diagnostic equipment, such as colonoscopy probes, providing a route to THz imaging inside the human body. Recent simulations have demonstrated that an on-chip THz sensor could be used for *in vivo* imaging of colon cancer tumor margins [12]. On-chip THz systems have previously been used for the spectroscopy of microfluidic systems [13] and for the recovery of fine detail in the THz spectra

of polycrystalline compounds [14], as well as to investigate THz plasmonics in low-dimensional semiconductors in the extreme environment of a dilution refrigerator [15].

Almost all of the previous work regarding on-chip THz-TDS has been performed using synchronous optical sampling techniques [2], which usually consist of a single pulsed laser beam split into two optical paths, with their relative arrival times at the detector varied using a retroreflector and a mechanical delay stage. In such schemes, the rate at which time-domain waveforms can be acquired is limited by the movement speed of the delay stage, and the duration of the time-domain measurement window is limited by the delay stage length. Additionally, the use of moving components may introduce uncertainties and noise into measured quantities [16]. In order to realize the significant potential of on-chip THz systems in sensing and medical imaging, the ability to perform real-time THz-TDS measurements at video rates is strongly desired [5]. Asynchronous optical sampling (ASOPS) [17–19] is an alternative technique which can be applied to THz-TDS measurements, making use of two different lasers with a small offset in their repetition rates. This offset causes the relative time delay between successive pulses produced by the two lasers to vary, allowing time-resolved measurements to be recorded without the need for mechanically moving components, thereby eliminating associated limitations on scanning speed. ASOPS has been successfully applied to a variety of free-space THz-TDS systems for both spectroscopy [19] and imaging [20]. However, the application of ASOPS measurement techniques to on-chip devices remains relatively unexplored. Previously, ASOPS measurements of an on-chip device have been used to create a laser-based vector network analyzer [21], in which the device consisted of a coplanar waveguide (CPW) structure patterned onto a gallium arsenide (GaAs) substrate. A gap in the center conductor of the CPW acted as a photoconductive switch for THz generation, with THz detection performed by electro-optic sampling (EOS) inside the GaAs substrate. Typical measurement times of several hours were reported using this system, with a peak spectral dynamic range of approximately 50 dB.

Here, we present ASOPS measurements of an on-chip THz device with integrated photoconductive switches for THz signal excitation and detection, achieving a spectral dynamic range of 50 dB for measurement times as short as 100 ms, and up to 88 dB for measurements of 500 s. We demonstrate that ASOPS can accurately acquire THz waveforms from on-chip systems by comparison with synchronous optical sampling. We explore the dynamic range of ASOPS measurements with on-chip devices as a function of measurement time, demonstrating the ability to perform THz time-domain measurements at video rates (20 - 100 Hz), with sufficient dynamic range to underpin future real-time THz spectroscopy measurements with these devices.

2. Methods

A schematic diagram of the CPW device used in this work is presented in Fig. 1(a). Device fabrication was performed in the Leeds Nanotechnology Cleanroom, by first epitaxially-transferring [22–24] a 350 nm layer of low-temperature grown gallium arsenide (LT-GaAs) onto a 500 μm-thick quartz substrate. Two 70 μm × 70 μm squares of LT-GaAs were defined using UV photolithography, whereby excess regions of LT-GaAs were removed using a weak H_2SO_4:H_2O_2:H_2O (1:8:950 by volume) etch solution. The weak etch solution formed sloped LT-GaAs sidewalls suitable for overlaying the waveguide geometry and electrical contacts, which were defined using UV photolithography and subsequent deposition of a 10/100 nm-thick Ti/Au metallization. The width of the center conductor and the bias electrodes was 30 μm, with a gap of 20 μm between the center conductor and the ground planes. Gaps of 5 μm between the bias electrodes and the center conductor over the LT-GaAs squares formed 4 photoconductive switches, labelled SW 1 to SW 4 in Fig. 1(a). Each of the photoconductive switches could be used for either THz signal excitation or detection. The centers of the LT-GaAs squares were separated by a distance of 1.2 mm along the waveguide axis. An optical microscopy image of one of the LT-GaAs squares and the overlaid

metallization is shown in the inset of Fig. 1(a). The device was mounted on a printed circuit board with a 6-way wire-to-board connector used to interface with external hardware.
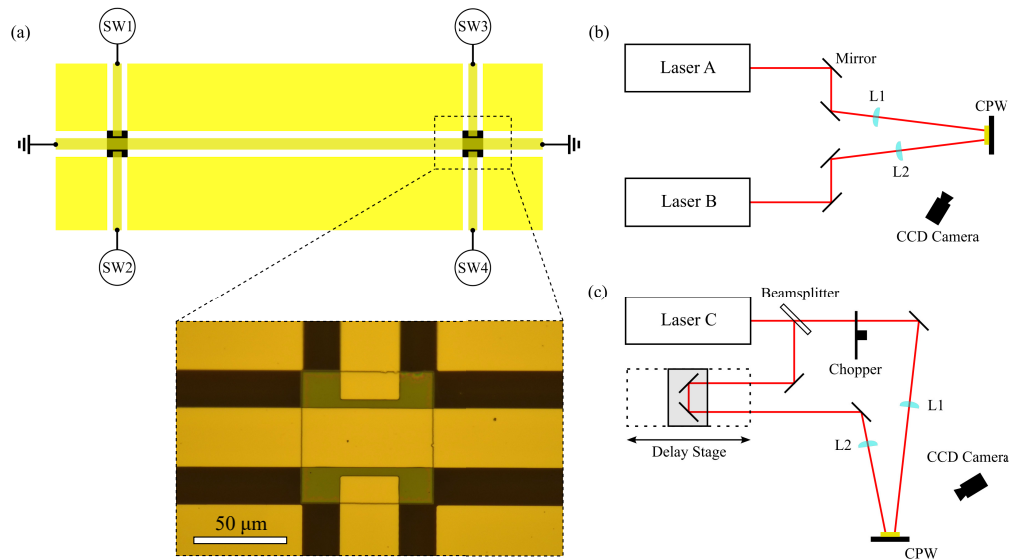
Fig. 1. (a) Schematic diagram of the CPW device, consisting of two LT-GaAs squares (black squares) connected by a central signal conductor, and the photoconductive switch bias electrodes (labelled SW1 to SW4). Inset is an optical microscopy image of one of the LT-GaAs squares and the overlaid metallization. (b) Schematic diagram of the optical layout used for ASOPS measurements of the CPW device. (c) Schematic diagram of the optical layout used for THz-TDS measurements with a scanning mechanical delay stage.

A commercially-available ASOPS laser system (Menlo Systems) was used in this work, consisting of two erbium-doped fiber lasers with second-harmonic generation units (Menlo Systems C-Fiber 780). Both lasers produced $< 100\,\text{fs}$ duration pulses with $780\,\text{nm}$ central wavelength and an average optical power of $45\,\text{mW}$. One laser in the pair (Laser A) was operated at a constant repetition rate $f_A = 100\,\text{MHz}$, whilst the second laser (Laser B) was locked to the repetition rate of Laser A but with a constant frequency offset $f_B = f_A + \Delta f$, where the frequency offset Δf was set at $100\,\text{Hz}$. The theoretical minimum time resolution of the ASOPS system is calculated from the difference in the reciprocal of the repetition rate of the two lasers, $1/f_A - 1/f_B = 10\,\text{fs}$. Practically, however, the experimental time resolution is limited by factors such as the laser pulse duration, the response time of the detection electronics, and the sampling rate of the data acquisition system; here the time-domain sampling rate was set to $10\,\text{MHz}$, resulting in a minimum time resolution of $100\,\text{fs}$.

The optical layout used for ASOPS measurements in this work is shown schematically in Fig. 1(b). The output from Laser A was used for THz pulse excitation, and the output from Laser B was used for THz detection. The beam from Laser A was routed onto the device via a 1 inch diameter, $200\,\text{mm}$ focal length lens, and was deliberately defocused to allow simultaneous illumination of SW1 and SW2. Coarse alignment of the beam onto the photoconductive switches was performed with the aid of a CCD camera. Fine alignment was then performed by applying a small DC bias of $+ 1\,\text{V}$ to both SW1 and SW2 using a Keithley 2400 Source Measure Unit, and beam position and defocusing were refined to maximize the photocurrent measured across the photoconductive switches. During all THz measurements presented in this work, the bias applied to both SW1 and SW2 was a constant $+ 20\,\text{V}$ DC. The beam from Laser B was tightly focused onto either SW3 or SW4 for detection of the transmitted THz pulse using a 1 inch diameter, $150\,\text{mm}$

focal length lens. The position and focusing of the detection beam was similarly optimized by maximizing the photocurrent across the detection switch under an applied DC bias of + 1 V. We note that no bias was applied to the detection switches during THz measurements, and only one detection switch was used to measure the transmitted THz signal at any time. Data acquisition was performed by the standard procedure for the commercial ASOPS system used in this work. A transimpedance amplifier (Femto DHPCA-100) was used to convert the induced photocurrent signal produced by the interaction of the THz pulse and the probe laser pulse at the detection switch into a voltage pulse, whilst also amplifying the signal, before detection using a fast analogue-to-digital converter. The amplifier was operated at a transimpedance gain of 10^6 V/A with a gain bandwidth of 1.8 MHz, where the gain setting was limited by the maximum output voltage (±1 V) of the amplifier at the peak of the THz transient. Further refinement of the excitation and detection laser beams was performed by maximizing the peak THz amplitude using real-time observation of the THz waveform.

To verify the time-domain waveforms obtained using ASOPS are comparable to those obtained by synchronous optical sampling techniques, a separate optical layout shown in Fig. 1(c) was used, designed to be as similar as possible to the optical layout used for ASOPS measurements. For this, a single, separate erbium-doped fiber laser with second-harmonic generation (Toptica FemtoFiber pro NIR) was used (Laser C), which produced <100 fs duration pulses with 780 nm central wavelength at a repetition rate of 80 MHz, with an average optical power at the laser output aperture of 143 mW. Using this separate laser allowed us to compare ASOPS measurements to a traditional THz-TDS system, whilst also having sufficient optical power for the THz generation and detection beams to be comparable with the ASOPS lasers. The output of Laser C was split into two beams by a 50:50 beamsplitter, with the THz excitation beam again simultaneously illuminating both SW1 and SW2 using a 1 inch diameter, 200 mm focal length lens. As before, a constant + 20 V DC bias was applied to both SW1 and SW2 during THz measurements. The THz detection beam was routed through a mechanical delay stage before being focused tightly onto SW3 or SW4 using a 1 inch diameter, 150 mm focal length lens. Laser alignment onto the device was optimized by the same procedure described previously for the ASOPS system, and the average photocurrent measured across each photoconductive switch was comparable to the ASOPS system. An optical chopper was positioned in the THz generation beam path, and a lock-in amplifier synchronised to the chopper frequency was used to measure the output signal from the detection switch.

3.   Results and discussion

Figure 2 presents a THz time-domain waveform obtained via ASOPS using the CPW device (black trace). The main transmitted peak of the THz pulse is observed at a time delay of 0 ps, with the subsequent oscillations starting at 21 ps occurring due to multiple overlapping reflections of the THz pulse from various parts of the CPW geometry. The THz group velocity in the waveguide was measured by swapping the photoconductive switches used for THz generation and detection without altering the optical alignment, resulting in a THz pulse propagating in the opposite direction along the waveguide. The difference in arrival time of the THz pulse between the forward- and reverse-propagating arrangements was 14.1 ps which, with an effective propagation length of 2.4 mm, equates to a THz group velocity of 1.7×10^8 m/s. The first reflection visible in the time-domain waveform at 21 ps corresponds well with the closest wire bond used to connect the device to the printed circuit board, which was 1.8 mm away from the nearest photoconductive switch (equivalent to a 3.6 mm round trip). The ASOPS measurement presented in Fig. 2 is the average of 5×10^4 individual time-domain traces, each with a 10 ms acquisition time (corresponding to a scan acquisition rate of 100 Hz), resulting in a total acquisition time of 500 s. The time-domain scan window was set to 40 ps in Fig. 2 to highlight the main features of the THz waveform. However, in principle the ASOPS system used here permits data acquisition

to be performed over a 10 ns duration time window at the same scan acquisition rate, where the maximum size of the time window is limited only by the reciprocal of the repetition rate of Laser A. Presented alongside the ASOPS measurement is a time-domain waveform obtained by synchronous optical sampling using the same CPW device (red trace), for comparison. The total time taken to acquire this 40 ps time-domain window was 480 s, using a lock-in time constant of 200 ms and sampling period of 1.2 s, with a time resolution of 100 fs to match the ASOPS measurement. Both waveforms are in good agreement with each other, displaying the same temporal structure of the main pulse and subsequent characteristic oscillations from the device geometry, demonstrating that the ASOPS technique can be used to acquire accurate time-domain waveforms from on-chip THz systems. The Fourier transform spectra of the two waveforms are presented in the inset of Fig. 2. To assess the frequency content of the main pulse without the influence of Fabry-Pérot effects from THz reflections at the ends of the device geometry, and to avoid spectral leakage effects from the edges of the time window [25], a 25 ps-wide Hann window centered at 0 ps was applied to both time-domain traces. Both spectra peak at zero frequency and display a similar monotonic decrease in amplitude with increasing frequency down to the noise floor of the measurement, consistent with spectra obtained from other on-chip THz devices [11] where the bandwidth is limited by propagation losses along the waveguide. Small variations in the spectra between the two setups may be due to differences in pulse duration between the two laser systems and variations in the precise optical alignment of each setup. We note that the total acquisition time of the scanned delay-line measurement was designed to match that used in the ASOPS measurement, for the purpose of comparing the waveforms measured by the two techniques, and is not as an indication of the maximum scan rate attainable from such synchronous optical sampling methods; for example, scan rates up to 20 Hz have been demonstrated using fast-scanning delay units [26].

Having established that ASOPS produces THz-TDS measurements in good agreement with synchronous optical sampling methods for on-chip THz devices, we now explore the performance of the ASOPS technique with our device as a function of measurement acquisition time. Dynamic range (DR) is a commonly used metric to assess the performance of a THz-TDS system [2,27], often used to describe the maximum absorption strength of a spectral feature that can be discerned by the system in question. It can be defined in units of decibels as

$$\text{DR} = 20 \log_{10} \left(\frac{E_S(\omega)}{N_{RMS}} \right), \tag{1}$$

where $E_S(\omega)$ is the frequency-dependant amplitude of the signal spectrum and N_{RMS} is the root mean square (RMS) value of the background noise spectrum. Figure 3(a) presents the time-domain waveform acquired by a 500 s ASOPS measurement (red trace) alongside the background noise in the time-domain (black trace, amplitude multiplied by a factor of 500 for clarity). The background noise was quantified by acquiring another ASOPS waveform over the same 500 s measurement period but at a time delay of 100 ps before the arrival of the main THz pulse. The frequency spectra of the signal and noise measurements are presented in Fig. 3(b), obtained by Fourier transforming the time-domain traces in Fig. 3(a). As before, a 25 ps-wide Hann window was applied to both signal and noise time-domain traces, shown by the dashed green line in Fig. 3(a). The noise floor in the frequency-domain was calculated as the RMS amplitude of the noise spectrum between 100 GHz and 4 THz, shown by the solid black line in Fig. 3(b). The frequency-dependent dynamic range for an ASOPS measurement with 500 s acquisition time, calculated using the data from Fig. 3(b) in Eq. (1), is represented by the solid red line in Fig. 3(c). The dashed red line in Fig. 3(c) represents the dynamic range of the 500 s measurement calculated using the frequency-dependent noise spectrum in place of N_{RMS} in Eq. (1), for comparison. The two techniques for quantifying dynamic range agree well down to a frequency of 150 GHz, below which low-frequency noise causes the dynamic range to decrease
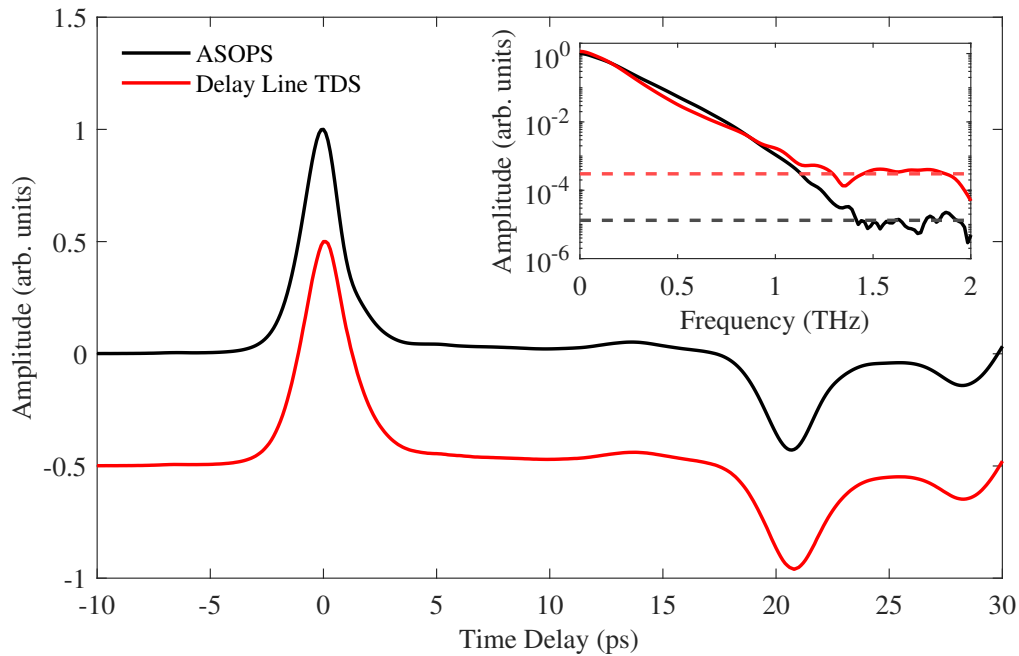
Fig. 2. THz time-domain waveform acquired by asynchronous optical sampling with the CPW device (black curve), alongside the waveform obtained from the same device using a separate THz-TDS system where the time delay is varied using a retroreflector and a mechanical delay stage (red curve, offset vertically for clarity). Inset are the Fourier transform spectra of the time-domain traces, where the dashed lines represent the noise floor of the corresponding measurement.

when using the frequency-dependent noise spectrum in the calculation. The low-frequency noise is likely to be caused by pickup of environmental noise, since the device used in this work had minimal shielding from the local electromagnetic environment. Shielding of the device may thus provide further improvements to the dynamic range of future on-chip THz measurements with ASOPS. In our subsequent analysis and discussion we will refer to the dynamic range calculated with N_{RMS}, which demonstrates the dynamic range trends without the influence of oscillations introduced by the noise spectrum. We also refer to the peak dynamic range of our measurement as the dynamic range at 150 GHz, in agreement with the calculation using the frequency-dependent noise spectrum. Presented alongside the 500 s measurement in Fig. 3(c) are dynamic range calculations for measurement acquisition times of 2 s (purple trace) and 10 ms (blue trace). For the 2 s-duration measurement the signal and noise spectra are the average of 200 individual time-domain traces each, whilst 10 ms corresponds to a single signal and noise time-domain trace. The magnitude of the dynamic range at a given frequency and the usable spectral bandwidth are observed to increase with increasing acquisition time. For all acquisition times the dynamic range demonstrates a monotonic decrease with increasing frequency, matching the shape of the THz spectrum, with frequency components extending out to 0.8 THz in the 10 ms measurement and up to 1.4 THz in the 500 s measurement before hitting the noise floor.

To elucidate these trends further and explore the usability of ASOPS measurements of integrated on-chip devices for THz sensing and imaging applications [12], Fig. 4 presents the dynamic range at four representative frequencies in the device's experimental bandwidth for a range of acquisition times between 10 ms and 500 s. For each acquisition time, the frequency-dependent dynamic range was extracted by the method described above and as depicted in Fig. 3. For

each of the four frequencies the dynamic range increases linearly with increasing acquisition time (i.e., with an increasing number of averaged time-domain waveforms), with a maximum dynamic range of 88 dB observed at 150 GHz for an acquisition time of 500 s. We note that the dynamic range of a typical commercial free-space ASOPS system is around 80 dB using a similar acquisition time and scanning rate [28], whilst previous on-chip ASOPS THz-TDS measurements achieved 50 dB dynamic range using measurement times of several hours [21], for comparison. We attribute the increase in dynamic range of our system compared to previous on-chip ASOPS THz-TDS measurements to our ability to directly measure the picosecond current pulse using a photoconductive switch integrated into the on-chip waveguide itself, rather than relying on the electro-optic effect in the device substrate for detection. We also highlight the difference in application of our device and the one described in Ref. [21]: the previous technique utilizes EOS to provide a movable probe position for signal detection, in order to realize a laser-based
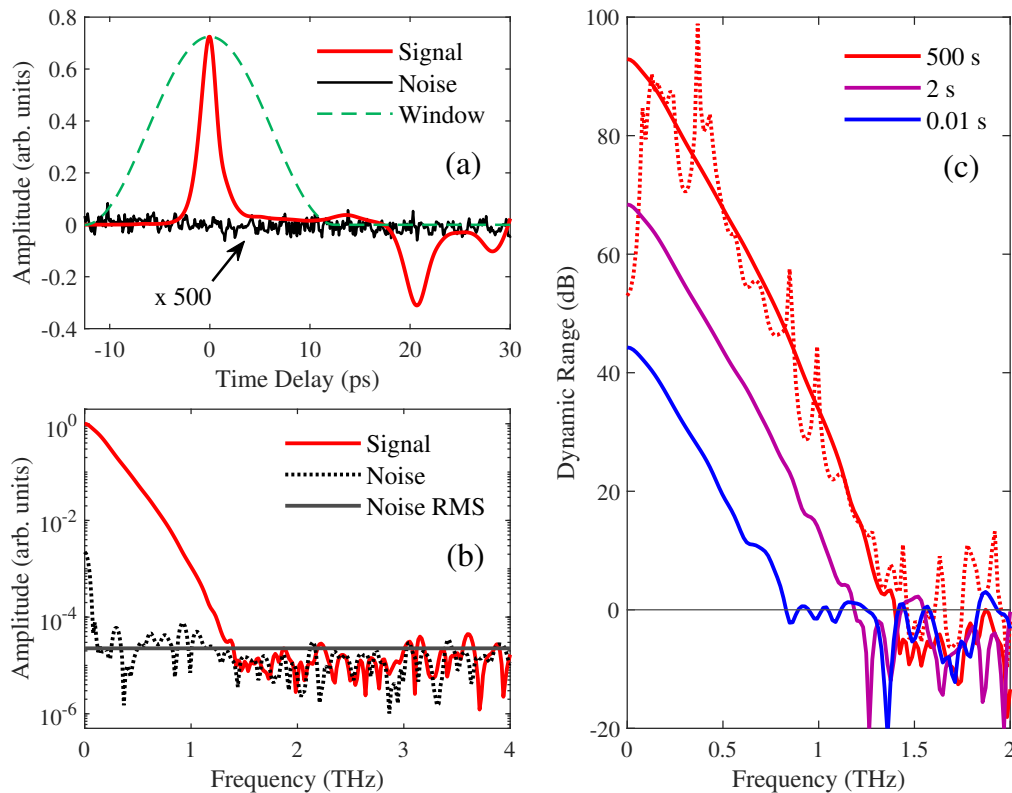
Fig. 3. (a) THz time-domain waveform obtained by a 500 s ASOPS measurement on a CPW device (red curve). The black curve is a 500 s ASOPS measurement obtained at a time delay of 100 ps before the arrival of the main THz pulse (with a + 100 ps offset along the horizontal axis, and with amplitude multiplied by a factor of 500, for clarity). The dashed green line depicts the window function used to analyze the spectral content of the waveforms. (b) Fourier transforms of the time-domain waveforms in panel (a) after windowing. The dashed black line is the Fourier transform of the noise waveform from panel (a), and the solid black line is the RMS amplitude of the noise spectrum. (c) Frequency-dependent dynamic range of on-chip ASOPS measurements with varying acquisition times, calculated using the RMS noise floor. The dashed red line represents the dynamic range of the 500 s measurement calculated using the frequency-dependent noise spectrum (dashed line in panel (b)) rather than the RMS noise floor, for comparison.

VNA measuring reflection coefficients and scattering parameters of a device under test; our device employs photoconductive switches integrated directly into the on-chip waveguide which, whilst having a fixed probe position, can provide rapid and high dynamic range spectroscopic measurements of a range of overlaid analytes. Linear fits to the data in Fig. 4 produced gradients of 9.6 ± 0.4 for the 150 GHz, 300 GHz, and 600 GHz data, and a gradient of 9.1 ± 0.5 for the fit to the 800 GHz data, where the errors are the 95 % confidence intervals on the fits. These fit coefficients demonstrate that the dynamic range increases proportionally with acquisition time at frequencies up to at least 600 GHz. To assess the applicability of integrated on-chip THz systems for real-time sensing and imaging, we define the effective sensing rate (ESR) as the rate at which N individual ASOPS time-domain waveforms can be averaged to produce a sample trace, ESR $= 1/Nt_s$ where $t_s = 10$ ms is the time taken to acquire a single time-domain measurement. The ESR is therefore equal to the reciprocal of the total acquisition time for the time-domain waveforms used to extract the data in Fig. 4, as shown by the upper horizontal axis in Fig. 4. For acquisition times of $50 - 10$ ms, we demonstrate the ability to perform video-rate acquisition of time-domain waveforms from on-chip THz systems with ESR values of $20 - 100$ Hz, respectively, and a dynamic range of over 40 dB at the peak frequency of 150 GHz.

The video-rate data acquisition demonstrated in this work opens a route to real-time THz sensing of small volume analytes [13,29], as well as imaging via modalities using scanned THz waveguides integrated with resonant sensing structures. For example, Park *et al.* [12] recently simulated that THz sensor devices, comprising a planar Goubau line waveguide with a
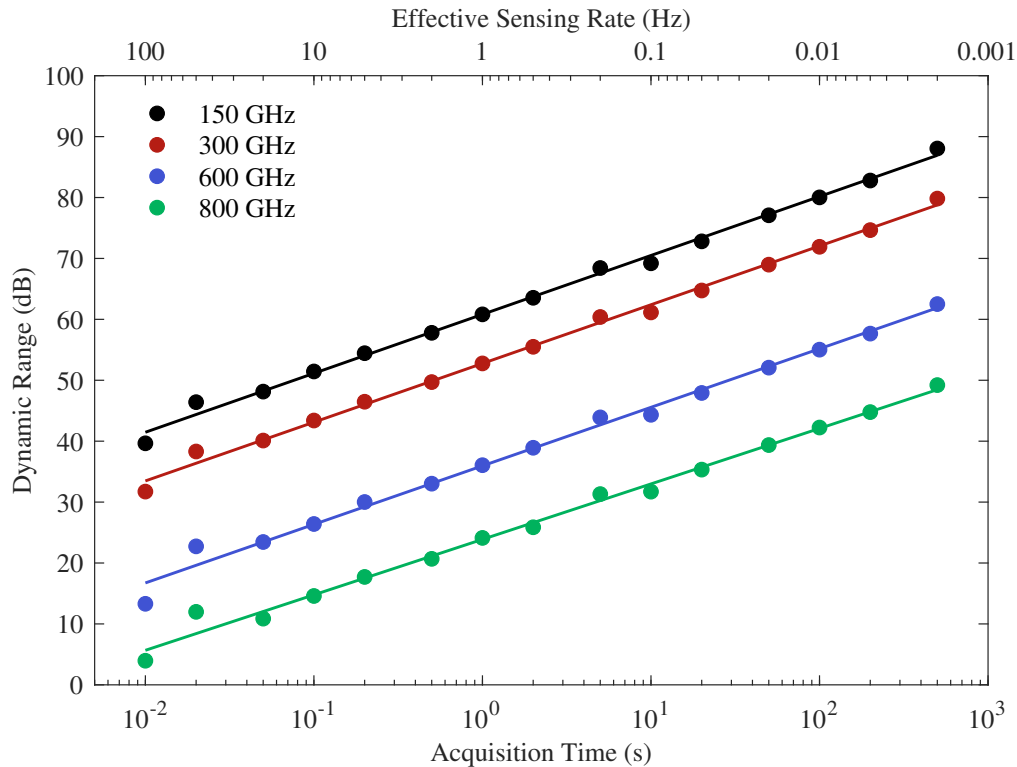
Fig. 4. Dynamic range of on-chip ASOPS measurements for four representative frequencies in the device bandwidth, as a function of the measurement acquisition time and it's corresponding effective rate of measurement for sensing and imaging applications. Lines are linear fits to the data to highlight the trends.

capacitively-coupled split-ring resonator (SRR), could be used to differentiate between cancerous and healthy tissues when scanned across the tissue boundary, using the resonant frequency shift induced by dielectric loading of the SRR as the contrast mechanism. The SRR in the device was predicted to have an absorption depth of 13 dB at the resonant frequency of 600 GHz, which is within the detectable range at video-rate ESR demonstrated using the THz-frequency CPW in this work. Whilst differences in waveguide geometry may affect the dynamic range and bandwidth of transmitted THz radiation [13], the nature of resonant structures, such as SRRs, means the resonant frequency can be straightforwardly tuned to a region of sufficient dynamic range within the device bandwidth by scaling the dimensions of the resonator [30].

4. Conclusion

We have demonstrated video-rate THz-TDS data acquisition using ASOPS measurements of on-chip THz waveguide devices, which have integrated photoconductive switches for the generation and detection of THz pulses. The integrated nature of both the THz source and detector permits data acquisition to be performed orders of magnitude faster than schemes utilizing electro-optic sampling for detection, demonstrating effective sensing rates up to 100 Hz with a peak dynamic range of 40 dB. Over longer measurement acquisition times of several hundred seconds, we observe a peak dynamic range of up to 88 dB. The work presented here provides a route to real-time on-chip THz-TDS measurements at video rates for sensing and imaging applications.

Disclosures. The authors declare no conflicts of interest.

Data availability. The data associated with this paper are openly available from the University of Leeds Data Repository in Ref. [31].

References

1. P. U. Jepsen, D. G. Cooke, and M. Koch, "Terahertz spectroscopy and imaging – Modern techniques and applications," Laser Photonics Rev. **5**(1), 124–166 (2011).
2. M. Koch, D. M. Mittleman, J. Ornik, *et al.*, "Terahertz Time-Domain Spectroscopy," Nat. Rev. Methods Primers **3**(1), 48 (2023).
3. A. D'Arco, M. Di Fabrizio, V. Dolci, *et al.*, "THz Pulsed Imaging in Biomedical Applications," Condens. Matter **5**(2), 25 (2020).
4. S. S. Dhillon, M. S. Vitiello, E. H. Linfield, *et al.*, "The 2017 terahertz science and technology roadmap," J. Phys. D: Appl. Phys. **50**(4), 043001 (2017).
5. A. Leitenstorfer, A. S Moskalenko, T. Kampfrath, *et al.*, "The 2023 terahertz science and technology roadmap," J. Phys. D: Appl. Phys. **56**(22), 223001 (2023).
6. B. Fan, V. A. Neel, and A. N. Yaroslavsky, "Multimodal Imaging for Nonmelanoma Skin Cancer Margin Delineation," Lasers Surg. Med. **49**(3), 319–326 (2017).
7. Q. Cassar, S. Caravera, G. MacGrogan, *et al.*, "Terahertz refractive index-based morphological dilation for breast carcinoma delineation," Sci. Rep. **11**(1), 6457 (2021).
8. O. B. Osman, Z. B. Harris, J. W. Zhou, *et al.*, "In Vivo Assessment and Monitoring of Burn Wounds Using a Handheld Terahertz Hyperspectral Scanner," Adv. Photonics Res. **3**(5), 2100095 (2022).
9. G. G. Hernandez-Cardoso, S. C. Rojas-Landeros, M. Alfaro-Gomez, *et al.*, "Terahertz imaging for early screening of diabetic foot syndrome: A proof of concept," Sci. Rep. **7**(1), 42124 (2017).
10. Z. D. Taylor, R. S. Singh, D. B. Bennett, *et al.*, "THz Medical Imaging: in vivo Hydration Sensing," IEEE Trans. Terahertz Sci. Technol. **1**(1), 201–219 (2011).
11. J. Cunningham, M. B. Byrne, C. D. Wood, *et al.*, "On-chip terahertz systems for spectroscopy and imaging," Electron. Lett. **46**(26), S34–S37 (2010).

12. S. Park, R. Tucker, E. Pickwell-MacPherson, *et al.*, "Design of a Split Ring Resonator Integrated with On-Chip Terahertz Waveguides for Colon Cancer Detection," Adv. Theory Simul. **5**(9), 2200313 (2022).

13. M. Swithenbank, A. D. Burnett, C. Russell, *et al.*, "On-Chip Terahertz-Frequency Measurements of Liquids," Anal. Chem. **89**(15), 7981–7987 (2017).

14. C. Russell, C. D. Wood, A. D. Burnett, *et al.*, "Spectroscopy of polycrystalline materials using thinned-substrate planar Goubau line at cryogenic temperatures," Lab Chip **13**(20), 4065–4070 (2013).

15. J. Wu, A. S. Mayorov, C. D. Wood, *et al.*, "Excitation, detection and electrostatic manipulation of terahertz-frequency range plasmons in a two-dimensional electron system," Sci. Rep. **5**(1), 15420 (2015).

16. M. Bieler, H. Füser, and K. Pierz, "Time-Domain Optoelectronic Vector Network Analysis on Coplanar Waveguides," IEEE Trans. Microwave Theory Techn. **63**(11), 3775–3784 (2015).

17. P. A. Elzinga, R. J. Kneisler, F. E. Lytle, *et al.*, "Pump/probe method for fast analysis of visible spectral signatures utilizing asynchronous optical sampling," Appl. Opt. **26**(19), 4303–4309 (1987).

18. T. Yasui, E. Saneyoshi, and T. Araki, "Asynchronous optical sampling terahertz time-domain spectroscopy for ultrahigh spectral resolution and rapid data acquisition," Appl. Phys. Lett. **87**(6), 061101 (2005).

19. R. Gebs, G. Klatt, C. Janke, *et al.*, "Highspeed asynchronous optical sampling with sub-50 fs time resolution," Opt. Express **18**(6), 5974–5983 (2010).

20. M. Beck, T. Plötzing, K. Maussang, *et al.*, "High-speed THz spectroscopic imaging at ten kilohertz pixel rate with amplitude and phase contrast," Opt. Express **27**(8), 10866–10872 (2019).

21. P. Struszewski and M. Bieler, "Asynchronous optical sampling for laser-based vector network analysis on coplanar waveguides," IEEE Trans. Instrum. Meas. **68**(6), 2295–2302 (2019).

22. E. Yablonovitch, T. Gmitter, J. Harbison, *et al.*, "Extreme selectivity in the lift-off of epitaxial GaAs films," Appl. Phys. Lett. **51**(26), 2222–2224 (1987).

23. E. Yablonovitch, D. M. Hwang, T. J. Gmitter, *et al.*, "Van der Waals bonding of GaAs epitaxial liftoff films onto arbitrary substrates," Appl. Phys. Lett. **56**(24), 2419–2421 (1990).

24. J. Cunningham, C. Wood, A. G. Davies, *et al.*, "Terahertz frequency range band-stop filters," Appl. Phys. Lett. **86**(21), 213503 (2005).

25. J. Vázquez-Cabo, P. Chamorro-Posada, F. J. Fraile-Peláez, *et al.*, "Windowing of THz time-domain spectroscopy signals: a study based on lactose," Opt. Commun. **366**, 386–396 (2016).

26. C. Hoberg, P. Balzerowski, and M. Havenith, "Integration of a rapid scanning technique into THz time-domain spectrometers for nonlinear THz spectroscopy measurements," AIP Adv. **9**(3), 035348 (2019).

27. W. Withayachumnankul and M. Naftaly, "Fundamentals of Measurement in Terahertz Time-Domain Spectroscopy," J. Infrared Millim. Terahertz Waves **35**(8), 610–637 (2014).

28. Menlo Systems, "TERA ASOPS," D-TERA_ASOPS-EN datasheet, June 2021.

29. M. B. Byrne, J. Cunningham, K. Tych, *et al.*, "Terahertz vibrational absorption spectroscopy using microstrip-line waveguides," Appl. Phys. Lett. **93**(18), 182904 (2008).

30. S. Park and J. E. Cunningham, "Determination of Permittivity of Dielectric Analytes in the Terahertz Frequency Range Using Split Ring Resonator Elements Integrated with On-Chip Waveguide," Sensors **20**(15), 4264 (2020).

31. C. D. W. Mosley, R. Tucker, J. P. R. Nixon, *et al.*, "Data associated with 'Asynchronous optical sampling of on-chip terahertz devices for real-time sensing and imaging applications'," University of Leeds Data Repository (2024), https://doi.org/10.5518/1535.